VERSITA

A new approach to define surface/sub-surface transition in gravel beds.

Heather Haynes[1], Anne-Marie Ockelford[2], Elisa Vignaga[1], William M. Holmes[3]

[1]Institute of Infrastructure & Environment, School of the Built Environment, Heriot-Watt University, Edinburgh, EH14 4AS, SCOTLAND h.haynes@hw.ac.uk

[2]Department of Geography, Loughborough University, Loughborough, LE11 3TU, ENGLAND

[3]Wellcome Surgical Institute, Institute of Neuroscience and Psychology, University of Glasgow, Glasgow, G61 1QH, SCOTLAND

Abstract

The vertical structure of river beds varies temporally and spatially in response to hydraulic regime, sediment mobility, grain size distribution and faunal interaction. Implicit are changes to the active layer depth and bed porosity, both critical in describing processes such as armour layer development, surface-subsurface exchange processes and siltation/sealing. Whilst measurements of the bed surface are increasingly informed by quantitative and spatial measurement techniques (e.g. laser displacement scanning), material opacity has precluded the full 3-D bed structure analysis required to accurately define the surface-subsurface transition. To overcome this problem, this paper provides Magnetic Resonance Imaging data of vertical bed porosity profiles. Uniform and bimodal (σ_g = 2.1) sand-gravel beds are considered following restructuring under sub-threshold flow durations of 60 and 960 minutes. MRI data are compared to traditional 2.5-D laser displacement scans and six robust definitions of the surface-subsurface transition are provided; these form the focus of discussion.

Key words: MRI, Laser Scanning, Stress History, Porosity

INTRODUCTION

The interaction between the surface and subsurface of a river bed has important implications for a number of research avenues ranging from armour layer development, grain entrainment probabilities, sealing/siltation processes of deposition and associated changes to hyporheic exchange. Sediment studies generally consider that the surface of the river bed comprises the 'active layer' in which sediment exchange between the bed and transported load

© AG template

occurs. This concept was first defined by Hirano (1971) and later improved by Parker (1991) and Parker *et al*. (2000) and is readily applied to research concepts such as static bed armouring (Parker and Sutherland, 1990), bars (Lanzoni and Tubino, 1999), patterns of longitudinal sorting in rivers (Hoey and Ferguson, 1994) and numerical modeling (e.g. HECRAS). Specifically, Parker relates the active layer to bed level variations and stratigraphy; in this way he defines the bed as divided in two regions: i) a surface active layer, and ii) a substrate located immediately below the active layer. To obtain the thickness of the active layer Parker assumes that this region does not have vertical structure and that the porosity is constant. This concept underpins the probability of entrainment model of Hassan and Church (1994), where the probability of entrainment is set constant in the active layer and decreases towards zero in the substrate. Their justification was related to the relative exposure of the grain, yet this is only a partial explanation as entrainment is strictly related to other bed structure variables including the interlocking of grains and their settlement in the vertical which have been proven to be temporally and spatially dynamic even under sub-threshold flow (e.g. Haynes and Pender, 2007). Hence, the model presented by Hassan and Church (1994) would benefit from re-evaluating Parker's assumptions by detailed measurement of vertical bed structure and porosity, as related to the present paper. As this would permit improved definition of active layer depth and the surface-subsurface transition as paramount to accurate sediment transport modelling, it is therefore surprising that these definitions have remained arbitrary for so long.

Regarding definition of active layer depth, on the one hand it has been argued that active layer thickness scales with a characteristic grain size associated with only the surface layer, such as the $1D_{90}$ (e.g. Parker, 1991; Kaless and Mao, 2011). Others propose that active layer processes affect a greater depth of the bed and use slightly larger dimensions, e.g. equivalent to $2D_{84}$ (e.g. Hoey and Ferguson, 1994; Wathen *et al.*, 1995;) or $2D_{max}$ (Aberle, 2007). Further, the issue of time-dependent evolution of bed structure and surface grain size distribution arises. For example, research by Marion and Fraccarollo (1997) quite clearly states that during armour layer development, the thickness of the active layer is controlled by the maximum grain size and porosity (p). In this manner, porosity is also highlighted to be a relevant indicator of vertical bed structure (Aberle, 2007) and yields useful insight into surface processes of colmation, sealing and armouring well known to affect the susceptibility of surface particles to entrainment, thereby affecting active layer definition. Thus, whilst there is demonstrated inter-dependence of surface layer processes, porosity and active layer depth, no universal definition of the transition between the surface and subsurface has been agreed.

Such controversy is largely underpinned by limitations in the measurement techniques available for bed structure analysis. Although in the past two decades the use of laser scanners has improved analysis of the bed surface structure (e.g. Nikora *et al.*, 1998, 2001; Aberle and Koll, 2004; Aberle, 2007; Measures and Tait, 2008), they are depth-limited due to the opacity of the bed material. Thus, information pertaining specifically to the subsurface structure remains limited to bulk-average statistics, commonly porosity and grain size distribution, as obtained from alternative methods such as freeze-coring, wax-sampling, flume-drainage etc. (e.g. Zimmerman *et al*., 2005; Sibanda *et al.*, 2000; Aberle, 2007). Not only do these data fail to capture subsurface spatial arrangement, but they are contingent on the arbitrary layer definition in order to undertake the bulk-averaging process. Thus, the issue to hand becomes one of bed structure measurement in the vertical dimension where data sets would, ideally, provide simultaneous measurement of porosity and bed geometry (Aberle, 2007), as crucial to defining the surface-subsurface transition.

New technologies are increasingly being sought for 3-D and 4-D spatio-temporal descriptors of bed structure. Most recently, this has culminated in successful trials of Magnetic Resonance Imaging (MRI) on sand-gravel sediments; these have yielded full 3-D bed structure data in a non-invasive manner (Kleinhans *et al*., 2008; Haynes *et al*., 2009). Whilst this embryonic research technique is not without its challenges, it has permitted the first high resolution data (0.3mm) appropriate to detailed structural analysis in the vertical dimension (e.g. porosity, grain size, imbrication, orientation, pivoting angle etc.). Application of this technique therefore appears highly beneficial in resolving the controversy surrounding definition of the surface-subsurface transition in a robust, quantitative and validated manner.

This paper aims to investigate improved definition of the surface-subsurface transition depth. Using beds of varying grain size distribution and temporal evolution of structure, 3-D MRI data is compared to more commonly employed 2.5-D laser displacement. Six definitions, based on porosity curve analysis, are presented herein and discussion focuses on the merits and failings of each definition, culminating in a robust conclusion.

1. EXPERIMENTAL SET UP

1.1 Experimental Set Up

Experiments were performed within a glass-sided flow-recirculating flume of rectangular cross-section (15m long x 0.3m wide x 0.45m deep). Turbulent boundary conditions were induced over a 2m section of coarse immobile sediment directly downstream of the flume inlet, with the remaining test bed comprising mobile sediments. Two grain size distributions (Table 1) were employed with equivalent median grain size (D_{50} = 4.8mm); these were a uniform gravel 4-5.6mm and a bimodal sand-gravel mixture with $\sigma_g = (D_{84}/D_{16})^{0.5}$ = 2.1. Given the sensitivity of the MRI to magnetic properties of sediments (Haynes *et al*., 2009) a sub-angular dolomite aggregate was employed.

	Grain size distribution (% by weight)							
	1-1.4 mm	1.4–2 mm	2–2.8 mm	2.8–4 mm	4–5.6 mm	5.6–8 mm	8-11.2 mm	11.2-16 mm
Uniform	-	-	-	-	100	-	-	-
Bimodal	10	10	15	12	8	31	10	4
	Statistics (mm)							
	D_{16}	D_{50}	D_{84}	D_{90}	D_{max}			
Uniform	4.2	4.8	5.3	5.4	5.6			
Bimodal	1.7	4.8	7.6	8.7	16.0			

Table 1: Grain size distributions and appropriate statistical measures of the mobile test sediments.

For each experiment a sediment–filled perforated box (160mm long x 105mm wide x 60mm deep) was placed in the centre of the flume bed 8m downstream of the inlet. Equivalent material was used to fill the remainder of test section, then the entire bed was screeded so that all sediments were flush with the top of the box. Perforations in the box ensured continuity of subsurface flow through the test section. Employing a bed slope of 1/200, the bed was exposed to two discrete flow periods below the threshold for grain entrainment: (i) an initial *bedding-in period* of 30 minutes duration removed any air pockets or unstable grains generated during the screeding process; and (ii) a prescribed *water-working period* of 60 or 960 minutes at discharge ~5l/s. The water-working period employed shear stress, τ, equal to 50% τ_{c50} (where τ_{c50} is the critical entrainment threshold for the median grain size) and translating as a dimensionless shear stress of ~0.024; this set-up precluded active sediment transport and restricted structural rearrangement to in-situ and local processes typical of inter-flood periods (e.g. Haynes and Pender, 2007); no bedforms were identified. Thus, we ensured that the focus

of the paper was on surface-subsurface definition applicable to a range of bed structures, without suffering the additional complexities associated with active armouring or colmation of the bed surface.

Following application of the prescribed water-working period, the bed was very slowly drained until only the residual water remained in the sample. The sample was then laser scanned (see Section 1.2) to determine the bed surface topography. The residual water was then used to freeze the grains to together; this permitted transfer into the MRI bore without disturbance to the sediment .The perforated box was placed within a slightly larger water-tight container and the frozen sediment was slowly re-flooded by a cold-water injection process; this method prevents sediment disturbance. Subsequent to complete thawing, an MR image sequence was applied in all three axial planes and post-processed using the procedure outlined in Section 1.3. Thus, comparative laser and MRI data were generated for a surface area 100mm (x-direction) by 100mm (y-direction) over a depth of up to 60mm. A total of 8 data sets (4 experiments using 2 techniques) were analyzed for the vertical porosity profile.

1.2 Laser Methodology

Bed topography measurements were captured using a *Micro Elipson* scanCONTROL2800 laser scanner. The sensor reads the reflected laser light to simultaneously provide the x (cross-stream) and z (vertical) co-ordinates of 1024 discrete points along the laser beam; this is then replicated on a CCD array for quantitative evaluation. For the present investigations, the x-direction resolution was 0.115 ± 0.005mm (accounting for lateral splay of the beam and bed roughness effects on the reflection) whilst, in the z direction the resolution was 0.239mm (as controlled by the CCD array). The downstream (y) resolution was 0.125mm; this was generated by moving the laser in the downstream direction via an *Arrick Robotics* stepper table set to a prescribed speed of 25 mm per second. Thus, bed topographic data took only 4 seconds to acquire. Post-processing then truncated the data set to a 100mm x 100mm area centered on the box; this resulted in 695 200 discrete elevation points being analyzed per experiment. Figure 1a shows an exemplar planform DEM of the sediment sample.

1.3 MRI Methodology

As the detailed MRI methodology can be found in Haynes *et al*. (2009), only the information salient to the present investigations are provided herein. The

facility employed was the Bruker 7T (Tesla) scanner of the Glasgow Experimental MRI Centre. Data were collected using a 3-D Rapid Acquisition Relaxation Enhanced (RARE) sequence for a sample volume x= 100, y = 100 and z = 60mm using water (H^1 nuclei) as the imaging media. Here, application of a radio-frequency (RF) pulse to the sample causes 'resonant excitation' of the nuclear magnetic moment (spin) of the H^1 nuclei placed within the magnetic field. Specifically, this occurs when the nuclei change energy state from spins aligned with the magnetic field to spins opposing it (or vice versa). Thus, following an RF pulse the spin coherences result in some transverse magnetization which creates an oscillating current with frequency relating to the precession of the spin; this is the MRI signal. For the experiments presented herein, a sequence of RF pulses at 90º and 180º to the direction of the magnetic field were employed at 0.3mm resolution in the x, y and z planes. Total image acquisition time was 21 hours. Figure 1b shows an exemplar single horizontal slice taken close to the surface grain crests (planform view).

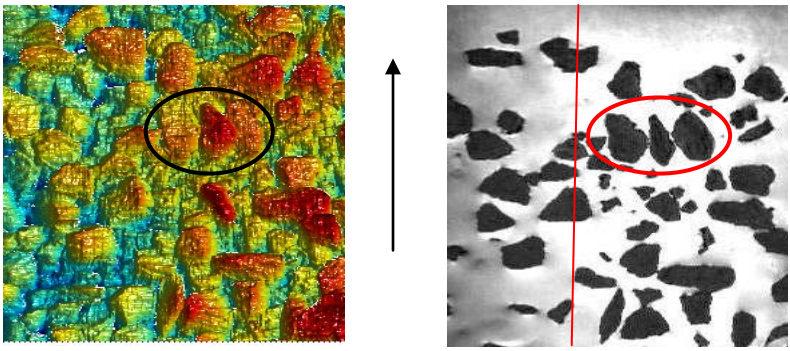

(a) **(b)**

Figure 1: Planform images of the bimodal sediment bed following 60 minutes of waterworking: (a) Laser scan data; (b) a *single* horizontal slice of the raw MRI image taken just below the most elevated grain crest such that only the most exposed grains are visible (black) in the surrounding fluid medium (white-grey). Flow direction is indicated by the black arrow on Figure (b). Circles highlight areas to demonstrate comparability of data and the red line shows the MRI slice extracted for use in Figure 2.

1.4 Data post-processing

As the raw laser data indicates the distance from the sensor to the local bed surface (Figure 1a), data was post-processed to consider only the range of elevations representing the bed surface topography. This provided arbitrary el-

evation data from the highest roughness crest down to the lowest layer tending to zero porosity; this is commonly assumed to correspond to the active layer depth when laser-based measurement techniques are employed (Aberle, 2007). Following the methodology of Aberle and Koll (2004) and Aberle (2007) data was post-processed in two stages: firstly, the surface Digital Elevation Model (DEM) was generated as one composed of 'pillars' whose ground-area is equal to the sampling resolution and height corresponds to the elevation measurement; secondly, the DEM was sliced into 100 layers and the porosity was then calculated for each layer based on the area of solid to the area of void. By taking the highest roughness crest as a datum (z_{max}) common to both the laser and MRI data, elevations were then normalized against the total depth of the MRI sample (z_t); this transformed laser-based elevation data into relative depth data (z) which could be directly compared to the MRI data in terms of z/z_t. Uncertainty analysis of the raw data indicates that variability in the x-direction resolution yields variability of porosity data less than 1.3% for the 100mm DEM area.

MRI data post-processing was then undertaken using the open source *ImageJ* software. Firstly, the total depth of the sample was determined (z_t) as defined from the base of the contained ($z = 0$) to highest grain crest on the bed surface (z_{max}). This truncated the field-of-view so as to focus analysis ($z_t < 60$mm) only on the bed (i.e. removing overlying water above the sample) and permitted the relative depth of each image slice (z/z_t) to be calculated. Secondly, image artifacts resulting from non-uniformity of the RF field away from the center of the RF coil had to be removed from the analysis. Only the data closest to the container walls and base were affected, totalling ~30% of the volume space. This truncation process also overcame well-known errors associated with higher porosity in the wall region, due to grains' poorer ability to imbricate here. Thirdly, binary thresholding (Figure 2) was used to separate sediments (no signal = black) from water-filled pores (signal = white/gray-scale). This applies the ISO DATA method to the brightness intensity of the image in the following way: firstly, the background (pore) signal and the average object (sediment) signal are calculated; secondly, these two values are summed then divided by two to determine the threshold value of the brightness signal. This yields a binary image thus allowing porosity (p) to be easily calculated as the volume of the voids (V_v) over total volume (V_t). Within the MRI data uncertainty in these values may stem from spatial averaging of the signal within each voxel. No uncertainty is associated with voxels which are 100% solid or 100% fluid (pore) hence errors can only be incurred at grain boundaries where voxels comprise part solid and part pore. As the binary thresholding is dependent on the brightness intensity of the raw data of each voxel, the ISODATA method is

most sensitive where the voxel comprises 50:50 solid:pore. Thus, two methods of uncertainty analysis were applied to the data. Firstly, statistical analysis of the standard deviation of the background (pore) and object (solid) were assessed for each slice. Using the sum of three standard deviations yields a maximum uncertainty of ±2% in the pore-solid data. Secondly, the sensitivity of the threshold was manually analysed by varying the brightness intensity bins ±1 to ±5; this was the range of gray-scale visual subjectivity. Here, data yields a range of 0.1-1.9% uncertainty. The maximum uncertainty (~2%) should be considered worst-case scenario, as this value is based on all grain boundary voxels having compositions close to the most sensitive ratio of 50:50 solid:pore. In reality, the proportion of fluid within boundary voxels will be highly variable, hence thresholding of the majority of voxels will be less sensitive and actual uncertainty far lower.

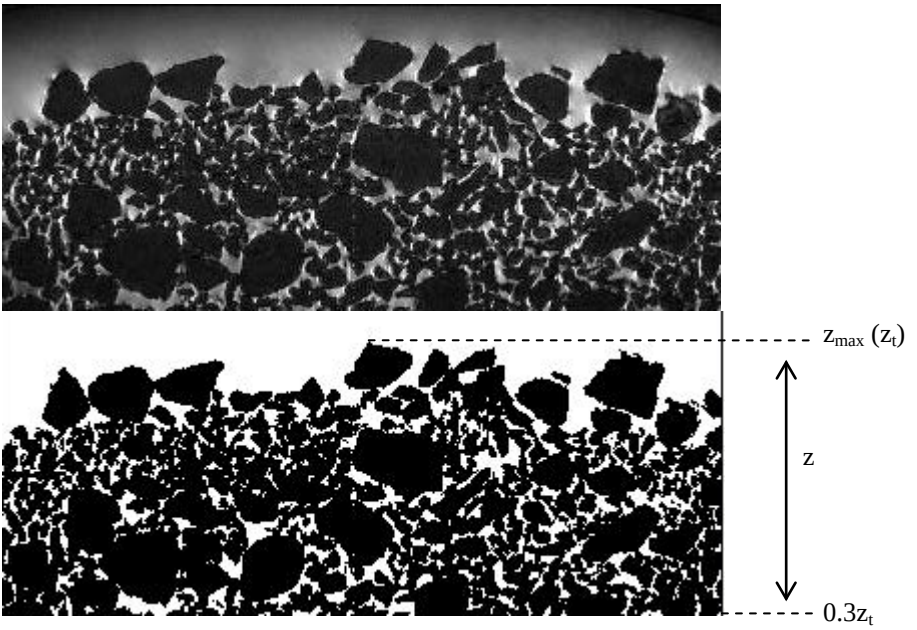

Figure 2: Vertical MRI images of the same bed as Fig. 1. Flow is from left to right showing: (a) single vertical raw-data slice in gray scale; (b) post-processed image using binary thresholding of grains (black) and pores (white). The field of view is truncated at $0.3z_t$ to remove the image region close to the base of the container, yielding image dimensions ~100mm by ~60mm.

With further regard to uncertainty in the porosity data, it is worth highlighting that the sample volume analyzed was set to the largest possible dimensions compatible with the bore diameter (152mm) of the MRI equipment.

With reference to the concept of Representative Elementary Volume (REV) in porous media, this minimizes the likelihood of fluctuations in the porosity value over the vertical profile. As Figure 2 clearly indicates, the sample area is both, significantly larger than a single pore and, includes a sufficiently high number of pores to suggest meaningful analysis of bed porosity. Excepting the surface-subsurface distinction, no macro-scale heterogeneity within the sample volumes was observed (e.g. defined strata in the subsurface or cross-channel bed patchiness). Thus, whilst small amplitude fluctuations in porosity between neighboring image slices are expected due to the natural random distribution of pore sizes, their magnitude may include slight uncertainty due to the REV or image post-processing resolution; this is elucidated upon later in the results section of the present paper.

Given the novelty and emerging use of MRI for sediment bed structure analysis, Table 2 provides a comparison of the technique against that of the more traditional laser-scanning methodology. This provides insight into the complexity, convenience, benefits and compromises of both techniques as appropriate to the present investigations.

Table 2: Comparison of laser and MRI techniques, as employed in the present investigations. Image resolution (*) for both techniques can be reduced to 50µm, however this compromises the spatial volume that can be imaged.

Method	**Laser**	**MRI**
3D image capability	Limited – 2.5D as restricted to surface-based measurement	Full - 3D spatial volume analysis
Image resolution*	~100µm	300µm
Time for data acquisition	Fast - 4 seconds for 695,200 data points	Slow - 21 hours for > 2.2 million data points
Complexity of data acquisition on instrument	Moderate – standard software user interface, performed by researcher.	Complex – trained MRI technical support required for sample calibration and image acquisition.
Complexity of software	Moderate – MATLAB license required	Simple – *ImageJ* is freely available for download
Data uncertainty	< 1.3%	< 2%
Restrictions	Bed surface must be drained Sample size/resolution dictated by the CCD	Material must be non-magnetic Sample must be contain magnetic nuclei in the fluid state Sample size dictated by the MRI bore

2. RESULTS AND DISCUSSION

In order to establish a definition of surface-subsurface transition, porosity data from laser and MRI experiments are analyzed in three different ways; these form the subheadings of this section, with the last section further subdivided. In total six definitions are provided and discussed. Whilst data could also be analyzed specifically in terms of bed structuring due to water-working duration and grade, these questions are considered out-with the main scope of the paper and are not considered specifically herein.

2.1 Where laser-based surface porosity tends to zero ($p = 0$)

Figure 3 clearly shows monotonic decay from $p = 1$ at the roughness tops to $p = 0$ at the lowest measured elevation. Data show that $p = 0$ occurs at relative depths of 0.71-0.79. Specifically, deeper surface-subsurface transitions are associated with: (i) graded beds, i.e. reflecting the greater surface roughness as commensurate with large D_{max} dimension; (ii) shorter water-working periods, which leave the bed surface poorly imbricated with a looser packing arrangements interjected by deeper pores (Haynes and Pender, 2007). However, when absolute depth is scaled to a larger characteristic grain size, the definition becomes sensitive to the grain size distribution; this precludes a generic definition of the surface-subsurface transition depth. To elucidate, $p = 0$ occurs at ~$2.2D_{max}$ in uniform beds but only ~$1.1D_{max}$ in graded beds. Whilst this latter descriptor disagrees with Aberle's laser-derived $2D_{max}$ definition of active layer thickness for graded beds, recalculating it based on D_{84} ($2.1\text{-}2.6D_{84}$ for uniform beds; $1.8\text{-}2.2D_{84}$ for bimodal beds) does support use of the arbitrary $2D_{84}$ value widely stated in sediment transport literature (e.g. Wathen *et al.*, 2005).

However, the laser can only read pores which are vertically aligned; this constrains the laser to a progressively smaller void with increased depth through the bed, thus explaining the 'perfect' monotonic decay trends. By failing to capture voids lying beneath grains (where the laser beam cannot penetrate), the absolute porosity of layers beneath the surface-most particles is therefore inaccurate. Therefore, whilst this method provides a measure of maximum pore depth and surface roughness geometry, we should not consider it 'porosity' *per se* as it cannot provide the 3-D data accurate absolute V_v/V_t measurement. It is therefore pertinent that we validate the laser-derived $p = 0$ against fully 3-D data for bed structure by way of MRI.

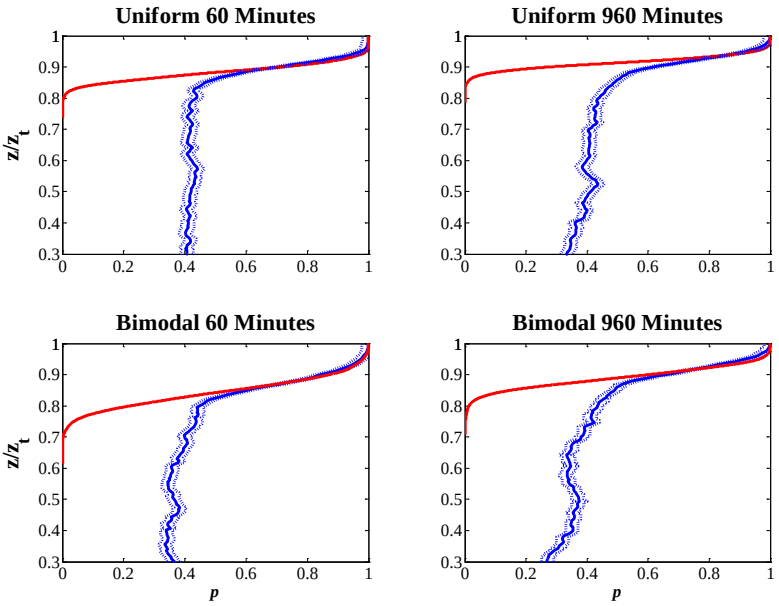

Figure 3: Vertical p profiles for uniform and bimodal beds (60 and 960 minute durations) given in terms of relative elevations, z/z_t. Laser-derived data is shown in red. MRI data in blue, including maximum uncertainty (dotted lines) of ±0.02. MRI profiles are truncated 30% above the base of the sample, due to image artifacts stemming from RF non uniformity close to the wall. Raw data are used to produce each profile ; no smoothing algorithm is employed.

2.2 Where laser and MRI porosity data diverge ($p_{laser} \neq p_{MRI}$)

Whilst line-of-sight issues causing $p \rightarrow 0$ are found in the laser data, the MRI data does not suffer the same problem. As such, porous granular materials should always show $p > 0$ throughout the vertical bed profile of the MR image, with $p \rightarrow$ constant for the subsurface. Where the data sets begin to diverge indicates the uppermost location where the laser does correctly measure the bed porosity; this occurs because the laser beam cannot 'bend' around a grain to analyse underneath the particle. It could therefore be argued that the subsurface can be defined by virtue of the fact that the laser cannot resolve what lies beneath its measured surface. To test the applicability of this definition, the divergence of laser and MRI data is explored.

Figure 3 clearly shows that surface layer porosity values are generally independent of measurement technique. The very minor differences in elevations (typically <0.3mm) are indicative of the different DEM resolutions em-

ployed; the larger (~1mm) mismatch of data for localised high elevations in the uniform bed (60 min.) is likely a facet of truncating the MRI planform area, compared to that of the laser scan (Section 1.4). At relative elevations 0.85-0.91of the sample depth, the laser and MRI begin to diverge. Thus, the surface-subsurface transition definition is ~$1D_{90}$ for uniform beds and 0.6-$1.0D_{90}$ for bimodal beds. Figure 3 shows that p values at this elevation lay within the range 0.6-0.8.

Whilst application of ~$1D_{90}$ definition of surface-sub-surface transition has some support from the literature (e.g. Parker, 1991), only the uniform bed supports this definition from $p_{laser} \neq p_{MRI}$. It would be highly unusual to describe the surface layer at values significantly below the characteristic D_{90}, as coarse grains would be expected to comprise the surface and active layer of a sediment bed; this definition does not, therefore, appear warranted for graded beds, so $p_{laser} \neq p_{MRI}$ cannot be considered a generic solution. In addition, such high p values would be unlikely at the surface-subsurface transition where grains would imbricate in all axial dimensions; this is true for all grain size distributions where porosities approximating to ~0.3-0.4 would be considered more typical (e.g. Fetter, 1988). Thus, the definition of surface-subsurface transition depth from $p_{laser} \neq p_{MRI}$ appears to be inappropriate and is made overly-complex by way of the need for both laser and MRI data sets.

2.3 Where a statistic of the first derivative of the MRI data (p') is used

Reviewing the MRI data on Figure 3 indicates that the reduction in bed porosity is progressive over relative depths from 1 to ~0.8; lower regions of the bed indicate more constant porosity values with oscillations in the data of magnitude similar to those found in Fetter (1998). Detailed analysis of individual oscillations indicates that most comprise multiple discrete data points (i.e. many adjacent image slices). Further, examination of the few instances where notable oscillations of p values occur, show that rapidly varying changes of p values up to 0.035 are recorded on Figure 3. As the magnitude of these larger fluctuations is greater than the maximum uncertainty caused by image resolution of the MRI data (<0.02), it supports the presence of natural variability in the porosity values of the subsurface for the given sample volume. As quantitative REV uncertainty analysis is precluded due to MRI facility constraints on sample size, it is therefore assumed that these fluctuations are indicative of a heterogeneous granular packing arrangement and manifest even on adjacent MRI slices as the cross-sectional area of an identified grain differs from one slice to the next slice. As such, attempts to apply

a smoothing algorithm to the porosity data would be inappropriate and further analysis of the raw MRI data is considered herein.

Of specific interest here is that the rate of change of porosity in the surface layer towards a more constant value in the subsurface can be better examined by the first derivative (*p'*) as derived by Equation 1. Here the difference in raw porosity values of adjacent horizontal slices of the MRI sequence (p_{i+1} - p_i) have been computed and divided by the relative distance between the slices ($\Delta z_{rel} = ((z/z_t)_{i+1} - (z/z_t)_i)$). Negative *p'* values indicate decreasing porosity with depth, whilst values tending to zero show a constant value of porosity (*p'* = 0).

$$p' = \frac{p_{i+1} - p_i}{\Delta z_{rel}} \qquad \text{Equation 1}$$

Four methods of surface-subsurface definition were trialled: (i) *p'* = -|max.|, which reflects the maximum rate of change in porosity over depth; (ii) the highest elevation at which increasing *p'* trends cross the statistical maximum uncertainty bound associated with constant porosity (i.e. *p'* = 0 - 3.8), defined as *p'* = -|uncertainty|; (iii) the highest elevation at which increasing p' trends fall within the observed oscillation band around constant porosity for each individual data set (*p'* = 0 - 1.6 to *p'* = 0 - 2.5), this is defined as *p'* = -|oscillation|; and (iv) the maximum elevation at which *p'* = 0, which indicates the elevation below which absolute porosity fluctuates around a constant value. A summary of these data are provided in Table 3 (together with comparison data from laser-related methods; Section 2.1 & 2.2).

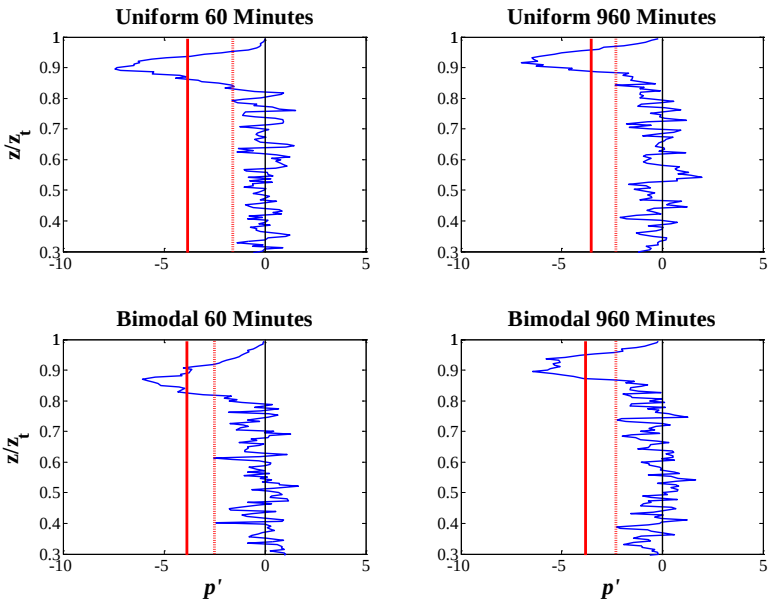

Figure 4: Vertical p' profiles derived from MRI data for uniform and bimodal beds (60 and 960 minute durations) given in terms of relative elevations, z/z_t. MRI profiles are truncated 30% above the base of the sample, due to image artifacts stemming from RF non uniformity close to the wall. The black line at x = 0 shows p' = 0. The solid red line shows p' = -|uncertainty| at x = -3.6, whilst the dotted red line shows p' = -|oscillations|. Raw data are used to produce each profile; no smoothing algorithm is employed.

Table 3: Surface-subsurface transition in terms of relative depth from the highest surface elevation. Information within parenthesis relates these data to the D_{90} and the D_{50} respectively; statistics provided are rounded to one decimal place.

	RELATIVE DEPTH in mm (relative to D_{90} and D_{50})			
	60 min. water-working		**960 min. water working**	
DEFINITION	**Uniform**	**Bimodal**	**Uniform**	**Bimodal**
Laser $p = 0$	**0.76** (2.5, 2.8)	**0.71** (1.9, 3.5)	**0.79** (2.1, 2.3)	**0.76** (1.6, 2.9)
Divergence $p_{laser} \neq p_{MRI}$	**0.90** (1.1, 1.2)	**0.85** (1.0, 1.8)	**0.91** (0.9, 1.0)	**0.91** (0.6, 1.1)
MRI p' = -|max.|	**0.90** (1.1, 1.3)	**0.87** (0.9, 1.6)	**0.92** (0.8, 0.9)	**0.89** (0.7, 1.3)
MRI p' = -|uncertainty|	**0.86** (1.5, 1.7)	**0.82** (1.2, 2.1)	**0.89** (1.1, 1.3)	**0.87** (0.9, 1.6)
MRI p' = -|oscillation|	**0.84** (1.7, 1.9)	**0.81** (1.2, 2.3)	**0.88** (1.2, 1.3)	**0.87** (0.9, 1.6)
MRI p' = 0	**0.82** (1.9, 2.2)	**0.79** (1.4, 2.6)	**0.79** (2.1, 2.3)	**0.79** (1.3, 2.4)

Firstly, using p' = -|max.| yields shallow surface-subsurface transition depths (0.7-1.1D_{90}), roughly equivalent to those calculated from $p_{laser} \neq p_{MRI}$ methodology. Further analyzing these data suggests that p' = -|max.| would under-

predict the transition depth, as the porosity continues to decrease (although at a progressively lower rate of change; Figure 4) towards deeper elevation depths; this deduction appears warrants as the subsurface would be expected to have more homogeneous porosity. In addition, the concerns raised for $p_{laser} \neq p_{MRI}$ are equally valid for p' = -|max.| data. This methodology is therefore considered inappropriate to defining the true surface-sub-surface transition.

Comparatively, application of p' = -|uncertainty| and p' = -|oscillation| provide a slightly deeper definition than p' = -|max.|. It is evident from Figure 4 that p' = -|uncertainty| appears arbitrary and unreflective of measured oscillations in the data set. As such, analysis herein focuses on p' = -|oscillation|. Here, the transition depths range from 0.9-1.7 D_{90} (Table 3) and appear more defensible when considered in terms of previous literature. However, there is clear influence of both grain size distribution and water-working on the results which precludes the definition being generic. This problem is exemplified in Figure 4; here the beds exposed to 960 minutes of water-working clearly have on p' = -|oscillation| at z/z_t of 0.87-0.88, yet the porosity continues to progressively decrease (i.e. $p \neq$ constant) to deeper depths until $p' = 0$ at z/z_t = 0.79. As the subsurface would be expected to illustrate near-homogenous porosity, use of the uppermost elevation at which the general trend for p' is increasing when p' = -|oscillation| is difficult to defend given this continuing trend over 3-10 subsequent layers of steadily increasing p' values deeper into the bed; this would suggest that the present method underpredicts the surface-subsurface transition depth for water-worked beds.

Of specific interest, are the data obtained via $p' = 0$ (i.e. $p \rightarrow$ constant); this method provides the deepest surface-subsurface transition depth and overcomes the p'= -|oscillation| problems. Crucially, data in Figure 4 indicate that this elevation demarks a clear transition from changing gradients in the surface layers to one of near-constant gradient in the subsurface. Where $z \leq z_{(p' = 0)}$ the absolute porosities of the subsurface are typically ~0.3-0.4 (Figure 3), in good agreement with the literature (e.g. Fetter, 1988). Conceptually, the choice of $p' = 0$ is defendable as water-working will rearrange the bed into its most stable packing arrangement; for a given grain size distribution, similarity of packing within the subsurface would be expected in a manner consistent with near-constant porosity. Table 3 provides strong support in that grade-specific consistency of $p' = 0$ data is found when normalization by the D_{90} is employed, here uniform beds yield surface-subsurface boundaries at ~$2D_{90}$, whilst bimodal beds tend to ~$1.3D_{90}$. However, the strongest support for this methods stems from near-generic $p' = 0$ data for all beds when normalized against the D_{50}.

Wider discussion of this methodology also indicates that for water-worked beds, this $p' = 0$ analysis provides data in line with those determined from the laser-based method of Aberle (2007); this is considered an important finding, as it provides some robust validation for use of surface-based laser scanning techniques in active layer depth examination for well water-worked beds. The statistics also translate well in terms of the alternative D_{84} characteristic grain scale; uniform beds indicate a surface-subsurface transition depth of $\sim 2D_{84}$, whilst the bimodal tends to $1.5D_{84}$. Thus, our data generally supports use of the arbitrary $2D_{84}$ statistic widely employed in previous active layer models and, in particular, tends to Wilcock *et al.*'s (1996) tighter definition of surface-subsurface transition depths at $1.7D_{84}$ in graded beds. Appropriate justification is provided to advocate that the MRI methodology of $p' = 0$ is a robust, repeatable descriptor of the surface-subsurface transition depth.

3. CONCLUSIONS

This paper compares and contrasts six definitions for the surface-subsurface transition depth in a gravel bed, based upon vertical porosity profile data. Each method provides mathematically-based approaches which are robust, repeatable and generic in application. Specifically, laser-based surface DEMs were contrasted with MRI-based 3-D data of the internal bed structure; these were then compared to common arbitrary definitions cited in the literature.

For water-worked beds, data clearly show that the MRI-based $p' = 0$ definition is the most generic descriptor of the surface-subsurface transition for the present research. It is highlighted that only 3-D MRI data can quantify pore volumes essential in obtaining absolute porosity data and it is illustrated that $p \rightarrow$ constant value in the subsurface ($\sim$0.3-0.4 in the present investigation). Thus, the results of this study: (i) provide robust, 3-D validation data important for applications pertaining to active layer definition in sediment transport research; (ii) illustrate the benefits of quantitative 3-D descriptions of porous media, which could be further exploited by sediment researchers.

Acknowledgements

This research was funded by a Research Grant award from the British Society of Geomorphology with additional support from The Carnegie Trust for The Universities of Scotland. The authors sincerely thank the technical

staff of GEMRIC and the School of Engineering at the University of Glasgow for their assistance in this research. Also, the reviews of the Associate Editor and an anonymous reviewer improved early drafts of the manuscript and we gratefully acknowledge this assistance.

References

Aberle, J. and K. Koll, (2004), Double-averaged flow field over static armour layers. **In:** M. Greco, A. Carravetta, and R. Della Morte (eds), *Proc. of the Intl. Conf. on Fluvial Hydraulics River Flow 2004 Naples, Italy,* Vol. 1, 225– 233.

Aberle, J., (2007), Measurements of armour layer roughness geometry function and porosity, *Acta Geophysica* **55,** 23-32.

Fetter, C.W., (1988), *Applied Hydrogeology (2nd Ed.)* Merrill Publishing Company pp.592.

Hassan, M. A., and Church, M. (1994). Vertical mixing of coarse particles in gravel-bed rivers: A kinematic model. *Water Resour. Res.*, 30(4), 1173–1185.

Haynes, H., E. Vignaga, and W.M. Holmes (2009), Magnetic Resonance Imaging of 3D River Bed Structure, *Sedimentology* **56**, 1961-1975.

Haynes, H. and G. Pender, (2007), Stress history effects on graded bed stability, *J. Hydraulic Engineering* **133**, 343-349.

Hirano, M. (1971). River bed degradation with armoring. *Proc., JSCE*, **195**, 55–65 (in Japanese).

Hoey, T.B. and R. Ferguson, (1994), Numerical simulation of downstream fining by selective transport in gravel bed rivers: Model development and illustration, *Water Resources Research* **30**, 2251-2260.

Kaless, G. and L. Mao, (2011), Numerical simulation of armour layer development under conditions of sediment starvation, *Proc. Convegno di Medio Termine dell'Associazione Italiana di Ingegneria Agraria, 22-24 Settembre 2011, Belgirate.*

Kleinhans, M. G., C. Jeukens, C. Bakker, and R. Frings, (2008), Magnetic Resonance Imaging of coarse sediment, *Sedimentary Geology* **208**, 69-78.

Lanzoni, S., and Tubino, M. (1999). Grain sorting and bar instability.*J. Fluid Mech.*, Cambridge, U.K., 393, 149–174.

Marion, A., and L. Fraccarollo, (1997), New conversion model for areal sampling of fluvial sediments, *J. Hydraulic Engineering* **123**, 1148-1151.

Measures, R. and S.J. Tait, (2008), Quantifying the role of bed surface topography in controlling sediment stability in water worked gravel deposits, *Water Resources Research* **44**, 4413-4430.

Nikora, V.I., D.G. Goring, and B.J.F. Biggs, (1998), On gravel-bed roughness characterization. *Water Resources Research* **34**, 517–527.

Nikora, V.I., D.G. Goring, I. McEwan, and G. Griffiths, (2001), Spatially averaged open channel flow over rough bed, *J. Hydraulic Engineering* **127**, 123-133.

Parker, G. (1991), Selective sorting and abrasion of river gravel. I: Theory, *J. Hydraulic Engineering* **117**, 131-149.

Parker, G. Paola, C. & S. Le-clair, (2000), Probabilistic Exner Sediment Continuity Equation for mixtures with no active layer. *J. Hydraulic Engineering* **126**, 818-826.

Parker, G., and Sutherland, A. J. (1990). Fluvial armor. *Int. J. of Hydr.Res.*, 28(5), 529–544.

Sibanda, E., I. McEwan, and A. Marion, (2000), Measuring the structure of mixed-grain-size sediment beds, *J. Hydraulic Engineering* **126**, 347-353.

Wathen, S.J., R.I. Ferguson, T.B. Hoey, and A. Werrity, (1995), Unequal mobility of gravel and sand in weakly bimodal river sediments, *Water Resources Research* **31**, 2087-2096.

Wilcock, P.R., G.M. Kondolf, W.V.G. Matthews and A.F. Barta, (1996), Specification of sediment maintenance flows for a large gravel-bed river, *Water Resources Research* **32**, 2911-2921.

Zimmerman, A., M. Coulombe-Pontbriand, and M. Lapointe, (2005), Biases of submerged bulk and freeze-core samples. *Earth Surface Processes & Landforms* **30**, 1405–1417.

Received December 1st 2011